Int. J. Multiphase Flow Vol. 16, No. 6, pp. 1071–1096, 1990
Printed in Great Britain.

0301-9322/90 $3.00 + 0.00

A FINITE DIFFERENCE COMPUTATIONAL MODEL OF ANNULAR FILM-FLOW BOILING AND TWO-PHASE FLOW IN VERTICAL CHANNELS WITH OFFSET STRIP FINS

G. D. MANDRUSIAK† and V. P. CAREY
Mechanical Engineering Department, University of California, Berkeley, CA 94720, U.S.A.

(*Received* 25 *May* 1989; *in revised form* 30 *April* 1990)

Abstract—This paper describes a detailed computational model of annular two-phase flow through offset strip fin heat exchanger geometries. In this model, a modified finite difference scheme is used to compute the velocity and pressure fields throughout the vapor core of the fin matrix. The vapor phase model is iteratively matched to a second finite difference model of the liquid film flowing along the channel walls. Three-dimensional interactions between the liquid film flowing along the prime and secondary surfaces of the matrix are also incorporated into the model. By solving the Navier–Stokes equation in the vapor phase, this model provides, for the first time, detailed local information about the shear stress and static pressure variation along the liquid film. This makes it possible to study the local variation of the heat transfer coefficient and wall shear stress all along the matrix. The model is validated against experimental data for two different offset fin geometries and then used to systematically study the effects of fin and channel geometry on two-phase transport. Special properties of two-phase flow through offset fin matrices discovered using the model are also described and the effects of these properties on the accuracy of previous annular flow models is discussed.

Key Words: finite-difference model, annular flow, boiling, offset fin surface

1. INTRODUCTION

Offset strip fin heat exchanger geometries of the type shown in figure 1 have been used in numerous single-phase heat transfer installations for many years. The excellent heat transfer properties of these heat exchangers have recently made them attractive for use in phase change heat transfer applications as well. Their high thermal efficiency makes them well-suited for numerous chemical processing and separation applications. In addition, their small size and weight make them ideal for use as evaporators and condensers in aircraft air-conditioning and refrigeration systems. If the advantages provided by the offset fin arrangement are to be fully realized in these applications, the two-phase operating characteristics of offset fin geometries must be well-understood.

Interest in applications of the type noted above has made the modeling of two-phase transport in offset fin geometries an important topic in multiphase flow research in recent years. Experimental studies of two-phase flow in offset fin matrices have shown that, in many applications, annular flow is the dominant flow regime over most of the channel (e.g. Carey & Mandrusiak 1986). As a result, most analytical models of two-phase flow have been developed for the annular flow regime. Film-flow models by Yung *et al.* (1980), Robertson (1982, 1984) and Carey & Mandrusiak (1986), for example, provide reasonable estimates of two-phase heat transfer coefficients over a wide range of flow conditions. For conditions in which nucleate boiling is a factor (for either annular or non-annular flow), models by Panitsidis *et al.* (1975), Chen *et al.* (1981) and Mandrusiak & Carey (1989) can be used to predict surface heat transfer performance. Information about the two-phase pressure drop characteristics of offset fin geometries can be obtained from adiabatic flow models of the type proposed by Carey & Bennett (1985) or Mandrusiak & Carey (1988).

†Current address: General Motors Corp., Troy, MI, U.S.A.

While existing models of annular flow in offset fin matrices are useful predictive tools, each includes idealizations which may limit the range of conditions and geometries over which they will be most accurate. Idealizations usually present in these models include:

(1) The shear stress along the interface of the liquid film flowing along the matrix walls is assumed constant all along the channel.
(2) With the exception of the film-flow model by Robertson (1984), droplet entrainment effects usually not included in the analysis.
(3) The static pressure gradient, when included in the liquid film analysis, is usually assumed favorable all along the channel.
(4) Transport in the liquid film is usually assumed similar to that for annular flow in continuous rectangular channels. The local changes in the liquid and vapor flow fields caused by the fins are usually not accounted for in the models.

Besides using many of these idealizations in their foundation, previous models have not provided a systematic way for quantifying the effects of channel geometry and fin arrangement on two-phase performance. In addition, existing models have supplied few details about how the liquid and vapor phases are distributed within the channel or how they interact with each other and the fins.

In the present study, annular two-phase flow in offset strip fin geometries is modeled from a more fundamental perspective. In contrast to previous efforts, the fluid mechanics of the vapor flowing through the cores of the matrix is analyzed in great detail. The vapor velocity and pressure fields are determined throughout the vapor core by numerically solving the governing equations for laminar or turbulent flow (as appropriate) within the fin matrix. These calculations provide, for the first time, an indication of the true variation of shear stress and static pressure along the interface of the liquid film flowing along the channel walls. This will permit a level of sophistication in modeling of transport in the liquid film which is significantly beyond that presented in earlier models.

In addition to the more detailed treatment of transport in each phase, the model of the liquid film developed here accounts for three-dimensional effects associated with the prime surface of the fin matrix. The special droplet entrainment characteristics which arise because of the interrupted nature of the channel walls are also included in the model.

After the details of the analytical treatment of each phase have been presented, the model is validated by comparing its predictions with experimental data available in the literature. The model is then used to theoretically quantify, for the first time, the effects of fin and channel geometry on two-phase transport in offset fin matrices. Some of the special properties of flow in offset fin geometries predicted by the computer model are also presented and their potential effect on the accuracy of previous models is described.

1.1. Overview of the model

In the model of annular flow to be presented in this paper, models of transport in the core- and film-flow regions are derived separately from the fundamental equations of fluid mechanics. These models are then joined together by imposing continuity requirements on velocity and shear stress all along the gas–liquid interface.

The vapor phase is modeled as a fully turbulent, periodically fully developed flow through a two-dimensional idealization of an offset fin array. The influence of entrained liquid on the vapor flow field was included by computing the effective fluid properties using homogeneous flow theory. The vapor model includes the effects of the irregular shape of the gas–liquid interface on the vapor flow domain and adjusts the boundary conditions to reflect the non-zero velocity of the interface of the liquid film.

The liquid film was treated using a weakly three-dimensional model formed by joining (along the corners of the channel) separate models of the film flowing along the prime and secondary surfaces of the matrix. This film model attempts to include the effects of the continual redistribution of the liquid phase along and around the walls of the fin matrix. The model includes the influence of both droplet deposition and entrainment and circumferential spreading of the liquid film by turbulent interfacial shear stresses on the rate of liquid redistribution around the matrix walls.

Since the streamwise variations in both the velocity and location of the gas–liquid interface depend on conditions in both phases, the exact computational boundaries cannot be specified *a priori*. Consequently, calculations in each phase proceed iteratively, with the output from one phase model serving as input to the other. Iterations continued until the location of the gas–liquid interface no longer changes and the velocity and shear stress vary continuously across the interface.

The equations governing the velocity and temperature fields in each phase and the techniques used to solve them will be presented in the following sections of this paper. For a more complete description of the two-phase flow model being developed here, the reader is referred to the thesis by Mandrusiak (1988).

2. NUMERICAL MODEL OF THE VAPOR PHASE

The analysis of the vapor phase traveling through the core of the fin matrix was simplified by introducing the following idealizations:

(1) The flow is periodically fully developed with a period of two fin lengths, i.e. profiles of all quantities across cross stream planes two fin lengths apart are identical.
(2) The core fluid is a mixture of pure vapor and discrete droplets entrtained from the liquid film flowing along the channel perimeter. The mean density, ρ_c, and viscosity, μ_c, of the two-phase mixture was determined using well-known homogeneous two-phase flow theory (Wallis 1969).
(3) The vapor core is isothermal at the saturation temperature of the test fluid. This eliminates the energy equation from the analysis of the vapor phase.

The irregular shape of the flow path formed by the fins of the matrix (figure 1) makes the vapor flow field very complex. As a result, the equations governing the velocity field are elliptic in nature and difficult to solve in their full, three-dimensional form. Because the model being developed here involves repeated calculation of the vapor velocity field, core-flow computations were performed using the two-dimensional idealization of the fin matrix of figure 1 shown in figure 2(a). This assumes that the prime surface has relatively little effect on the flow field in the vapor phase. While this is likely most accurate for channels having higher aspect ratios, it may also be reasonable for flow conditions in which fin effects strongly control the flow field in the matrix.

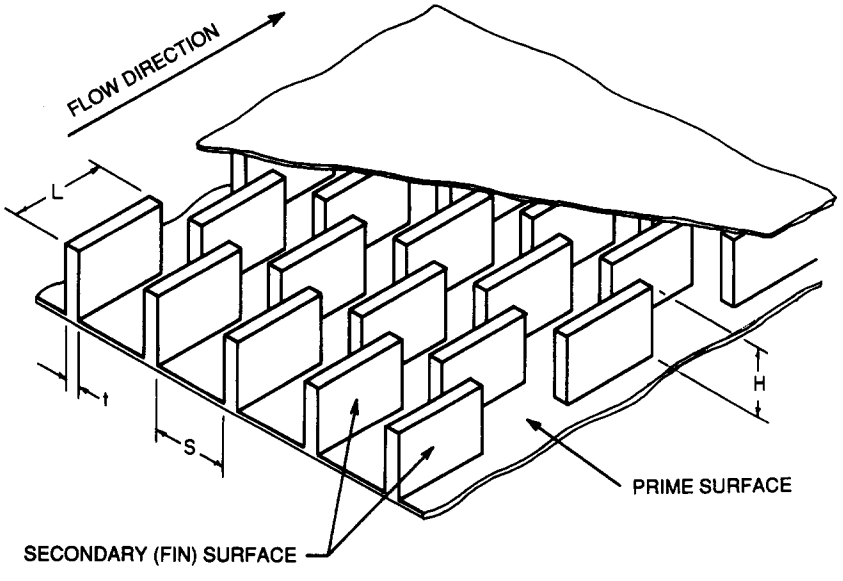

Figure 1. Diagram of a typical offset fin matrix.

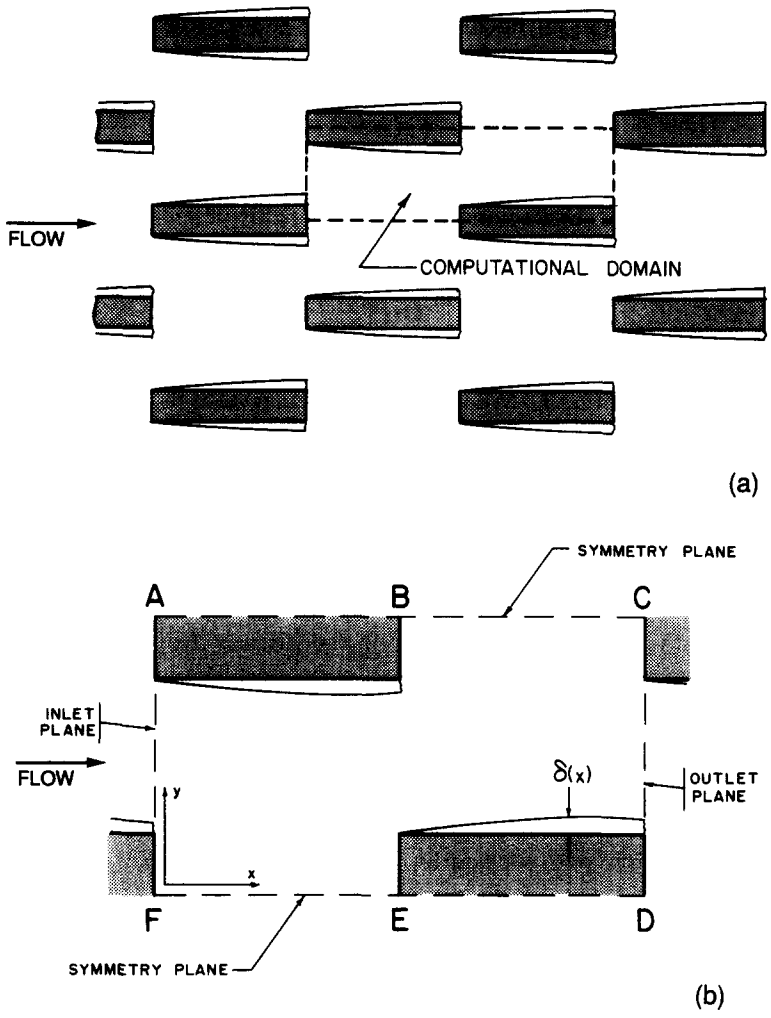

Figure 2. (a) Two-dimensional idealization of the offset fin surface. (b) Detailed diagram of the computational domain.

Assumption (1) allows the core-flow calculations to be performed over the representative unit cell ABCDEFA shown in figure 2(b). The equations governing the velocity field within this two-dimensional domain for either laminar or turbulent flow are:

$$\frac{\partial U_{ci}}{\partial x_i} = 0 \qquad [1]$$

and

$$\rho_c U_{ci} \frac{\partial U_{cj}}{\partial x_i} = -\frac{\partial P_c}{\partial x_j} - \rho_c g_j + \frac{\partial}{\partial x_i}\left[\mu_E\left(\frac{\partial U_{cj}}{\partial x_i} + \frac{\partial U_{ci}}{\partial x_j}\right)\right], \qquad [2]$$

where the subscript c denotes core-flow quantities. For laminar flow conditions, μ_E represents the effective molecular viscosity, μ_c, of the core fluid. For conditions in which the core flow is turbulent, μ_E represents the combined effects of molecular and turbulent viscosities:

$$\mu_E = \mu_c + C_\mu \rho \frac{k^2}{\epsilon}. \qquad [3]$$

The turbulent kinetic energy, k, and dissipation function, ϵ, in [3] are determined using the k–ϵ turbulence model:

$$\rho_c U_{ci} \frac{\partial k}{\partial x_i} = \frac{\partial}{\partial x_i}\left[\frac{\mu_E}{\sigma_k}\left(\frac{\partial k}{\partial x_i}\right)\right] + \mu_T \frac{\partial U_{ci}}{\partial x_j}\left(\frac{\partial U_{ci}}{\partial x_j} + \frac{\partial U_{cj}}{\partial x_i}\right) - \rho_c \epsilon \qquad [4]$$

and

$$\rho_c U_{ci}\frac{\partial \epsilon}{\partial x_i}=\frac{\partial}{\partial x_i}\left[\frac{\mu_E}{\sigma_\epsilon}\left(\frac{\partial \epsilon}{\partial x_i}\right)\right]+C_1\frac{\epsilon}{k}\mu_T\frac{\partial U_{ci}}{\partial x_j}\left(\frac{\partial U_{ci}}{\partial x_j}+\frac{\partial U_{cj}}{\partial x_i}\right)-C_2\rho_c\frac{\epsilon^2}{k}. \quad [5]$$

By using the standard k–ϵ model in these calculations, the turbulence in the core flow is being approximated as fully developed and isotropic. The conventional values of the coefficients appearing in [3]–[5] are summarized in table 1.

Table 1. Constants in the k–ϵ turbulence model

C_μ	C_1	C_2	σ_k	σ_ϵ
0.09	1.44	1.92	1.0	1.3

It is worth noting that, for the conditions examined here, the turbulent contribution to the effective viscosity, μ_E in [9] overwhelmed the contribution of molecular effects, μ_c, by as much as 2 orders of magnitude. The small size of the recirculation zones in the flow (see figure 9), the fine grid used along the impermeable boundaries and the (approximate) alignment of the flow with the grid lines reduced the effect of numerical viscosity on the calculations as well. For the conditions considered here, it is estimated that numerical viscosity was $<10\%$ of the turbulent viscosity, particularly in the region of interest along the gas–liquid interface.

The boundary conditions for [1]–[5] reflect the periodically fully developed nature of the vapor flow field. Here we take x to be the downstream coordinate, y is the coordinate normal to the fins and z is normal to the prime surface, with corresponding velocities U, V and W, respectively. Planes BC and FE in figure 2(b) are planes of symmetry, so that:

$$\left.\frac{\partial U_c}{\partial y}\right|_{y_{BC},y_{FE}}=0; \qquad V_c|_{y_{BC},y_{FE}}=0 \quad [6a]$$

and

$$\left.\frac{\partial k}{\partial y}\right|_{y_{BC},y_{FE}}=0; \qquad \left.\frac{\partial \epsilon}{\partial y}\right|_{y_{BC},y_{FE}}=0 \quad [6b]$$

In addition, profiles of U, V, k and ϵ and their associated streamwise derivatives across plane CD must match those across the inlet plane AF:

$$U_{ci}(x_{CD},y)=U_{ci}(x_{AF},y); \quad \left.\frac{\partial U_{ci}}{\partial x}\right|_{x_{CD}}=\left.\frac{\partial U_{ci}}{\partial x}\right|_{x_{AF}}, \quad [7a]$$

$$k(x_{CD},y)=k(x_{AF},y); \quad \left.\frac{\partial k}{\partial x}\right|_{x_{CD}}=\left.\frac{\partial k}{\partial x}\right|_{x_{AF}} \quad [7b]$$

and

$$\epsilon(x_{CD},y)=\epsilon(x_{AF},y); \quad \left.\frac{\partial \epsilon}{\partial x}\right|_{x_{CD}}=\left.\frac{\partial \epsilon}{\partial x}\right|_{x_{AF}}. \quad [7c]$$

The boundary conditions along the liquid film in figure 2(b) were chosen to ensure continuity of both velocity and stress across the gas–liquid interface:

$$\mu_c\left.\frac{\partial U_c}{\partial y}\right|_{y=\delta_F(x)}=\tau_{IF}(x) \quad [8]$$

and

$$U_c|_{y=\delta_F(x)}=U_{IF}(x); \quad V_c|_{y=\delta_F(x)}=V_{IF}(x)\approx 0 \quad [9]$$

The calculation of $U_{IF}(x)$ and $\delta_F(x)$ will be described in section 3.

The k–ϵ turbulence model given by [4] and [5] requires special treatment near impermeable boundaries. In its present form, the model is only valid in the fully turbulent region of the flow. To ensure the proper behavior of k and ϵ along the liquid film, the treatment proposed by Launder & Spalding (1974) was incorporated into the calculations. With this treatment, the generation terms

in the integrated form of [4] and [5] are modified near walls to reflect the turbulence "damping" which occurs in this region. In addition, the turbulent dissipation function, ϵ, is assigned a value determined by assuming that equilibrium turbulence (i.e. production = dissipation) exists near the boundaries:

$$\epsilon_q = \frac{C_\mu^{3/4} k_q^{3/2}}{\kappa y_q}. \qquad [10]$$

Finally, gradients of k normal to the walls are set to zero all along the impermeable boundaries to complete the boundary conditions on k and ϵ. (This last boundary condition ensures the proper behavior of the turbulent kinetic energy distribution as the edge of the fully turbulent region is reached.)

Equations [1]–[5] were solved using the SIMPLER algorithm [described in Patankar (1980)] in the TEACH-2E computer program described by Gosman & Iderian (1976). In this program, finite difference equations for each quantity (U, V, k etc.) are obtained by integrating the appropriate governing equation over control volumes centered around appropriately chosen grid locations in the flow. The resulting set of coupled, non-linear equations are then solved iteratively (using the SIMPLER algorithm) until all of the governing equations, [1]–[5], are satisfied to within a specified tolerance.

The encroachment of the liquid film on the vapor flow domain was included through a special grid-line treatment near the fin walls [figure 3(a)]. [The film thickness and grid spacing in figures 3(a, b) have been greatly exaggerated in comparison to the fin thickness for clarity.] If the liquid film occupied more than half a cell in the "true" configuration, the cell was incorporated into the boundary for the calculations (cell 1, for example). If less than half a cell was occupied by liquid, then the cell was included in the flow domain for the vapor core (cell 2, for example). In this way, the liquid film boundary shown in figure 3(a) was converted to the less exact, but more computationally feasible, shape shown in figure 3(b). During the calculations, the front (stagnation) and rear faces of each "step" in the film shape [figure 3(b)] were treated in the same way as the corresponding faces on the fins forming the matrix. Calculation of the interfacial shear stress along the streamwise face of each "step" proceeded as for a continuous, impermeable wall having a non-zero, streamwise velocity. Although this treatment introduces "artificial leading edges" along the gas–liquid interface, the film was too thin relative to the cross stream fin spacing to significantly affect the vapor core velocity and pressure fields. In addition, the variation in shear stress along the "stepped" interface of figure 3(b) did not differ markedly from that along a smooth fin wall.

The two-phase flow calculations required computing the vapor phase flow field many times for each set of conditions tested. Consequently, the grid used for the calculations had to be chosen to provide accurate shear stress and pressure field information in a reasonable amount of CPU time. Test calculations were performed with various grid densities [ranging from $23(x) \times 17(y)$ to $39(x) \times 33(y)$] before deciding upon a final grid of $33(x) \times 29(y)$ nodes. This algebraically-generated, non-uniform, rectangular grid yielded shear stress and pressure field information within $\pm 3\%$ of values computed using finer grids without consuming exhorbitant amounts of CPU time.

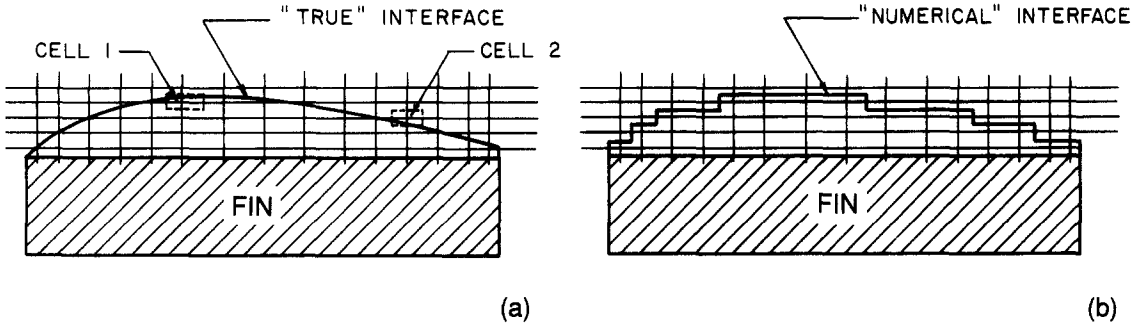

Figure 3. Treatment of an irregularly shaped liquid interface using a rectangular grid arrangement: (a) "true" film thickness variation; (b) approximation used for the calculations. The grid size and film thickness have been exaggerated in comparison to the fin thickness for clarity.

3. LIQUID FILM-FLOW MODEL

The fluid mechanics of annular flow in offset fin matrices is more complicated than flow in round tubes because of the discontinuous nature of the channel walls. The interruptions in the channel walls not only affect the distribution of the liquid film around the channel perimeter, but they also influence the droplet entertainment characteristics of the channel. In addition, the continual redistribution of the liquid film by the fins makes the governing transport equations more complicated than has been assumed in previous models.

In the discussion that follows, the distribution of the liquid phase within the matrix will be described in both qualitative and quantitative terms. The equations governing both momentum and energy transport in the liquid film will then be developed.

3.1. Liquid phase distribution

Although most previous models of annular flow have recognized the special nature of the walls of the fin matrix, treatment of the effects of the interruptions on flow and transport in the channel has varied widely. Yung *et al.* (1980) postulated that the liquid film was shed from the trailing edge of each fin as a continuous sheet. At the next downstream row of fins, this sheet was split by the leading edge of each fin and spread onto the fin walls to form a film of uniform thickness. Robertson (1984) suggested that the liquid film was dispersed into the vapor core as discrete droplets at the end of each fin. These droplets were then redeposited at a controlled rate along the walls of the next row of fins to form a film with a thickness that increased in the streamwise direction. More recently, Carey & Mandrusiak (1986) proposed that, for very short fins, surface tension pulled the liquid film to the prime surface at the downstream end of each fin. At the leading edge of the next row of fins, circumferential shear forces returned the liquid to the fin to create a film of uniform thickness.

In the present study, the treatment of wall discontinuity and its effects on the liquid film includes elements of each of the models described above. At the trailing edge of the fin, some of the film is assumed drawn to the prime surface by surface tension and the remainder is shed into the vapor core as discrete droplets [figure 4(a)]. Along the next downstream row of fins, liquid drawn to the prime surface from the previous row of fins is gradually swept onto the fin walls by interfacial shear forces. Additional liquid is transferred to the fin walls through droplet deposition from the vapor core [figure 4(b)]. The steps in this film transfer model will be cast in quantitative terms in the next section.

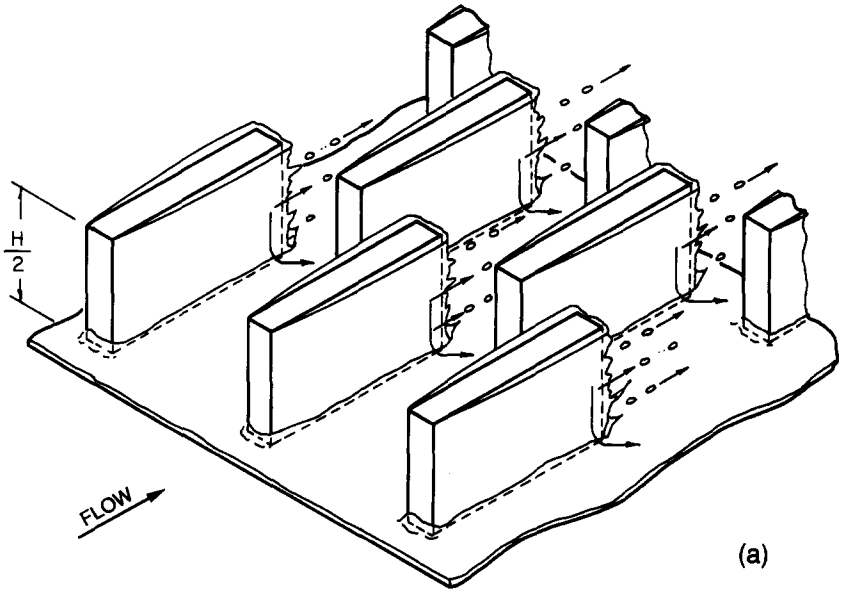

Figure 4a

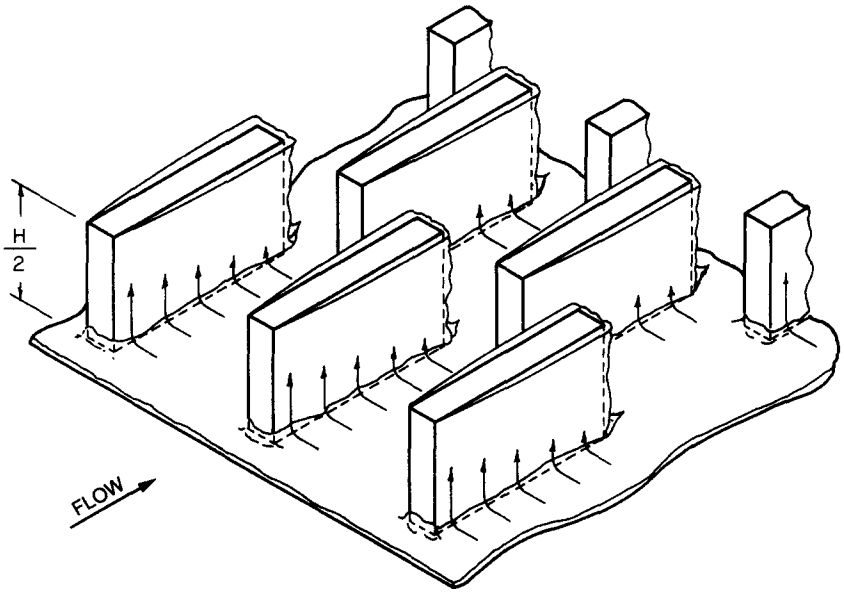

Figure 4b

Figure 4. Mechanism for exchanging the liquid film between successive rows of fins: (a) behavior at the trailing edge; (b) behavior at the leading edge.

3.2. Liquid film spreading

The mechanisms which spread the liquid film around the walls of the fin matrix are probably similar to those which sustain annular two-phase flow in horizontal tubes (against the tendency of gravity to stratify the two phases). The mechanisms active during annular flow in horizontal round tubes were described and evaluated in a review paper by Butterworth (1972). Of the basic mechanisms examined in that study, only one—lateral film spreading by circumferential shear stresses—is expected to be active in the flow situation being considered here. This mechanism is consistent with that proposed by Carey & Mandrusiak (1986) and was found by Butterworth (1972) to be one of the dominant mechanisms active in round tube flows as well.

To quantify the rate at which the liquid film is spread around the channel walls, basic elements of a model of annular flow in an eccentric annulus proposed by Butterworth (1968) were adapted to the present flow situation. Consider "unfolding" the liquid film flowing along the walls of the fin matrix to form the two-dimensional domain shown in figure 5. If a mass balance is performed on a segment of the liquid film, the following equation is obtained:

$$\frac{\partial \Gamma_x}{\partial x} + \frac{\partial \Gamma_z}{\partial z} = 0. \qquad [11]$$

The quantities Γ_x and Γ_z represent mass flow rates per unit width in the streamwise and circumferential directions, respectively. By analogy with other transport processes, Butterworth (1968) suggested that Γ_z was related to its streamwise counterpart, Γ_x, by

$$\Gamma_z = -\beta^2 \frac{\partial \Gamma_x}{\partial z}. \qquad [12]$$

The quantity β^2 represents a film spreading coefficient and has the dimensions of length. For round tubes, Butterworth (1968, 1972) found that β^2 did not vary strongly with either flow conditions or tube size, and ranged in value from 3 to 20 mm. In the present study, the optimal value of β^2 also appeared to be independent of flow conditions, but seemed to vary somewhat with channel geometry. As will be seen, good agreement between model predictions and available data was obtained when β^2 was approximated by

$$\beta^2 = \tfrac{1}{10}(S + H).$$

For the geometries considered in the present study, β^2 was about 3 mm.

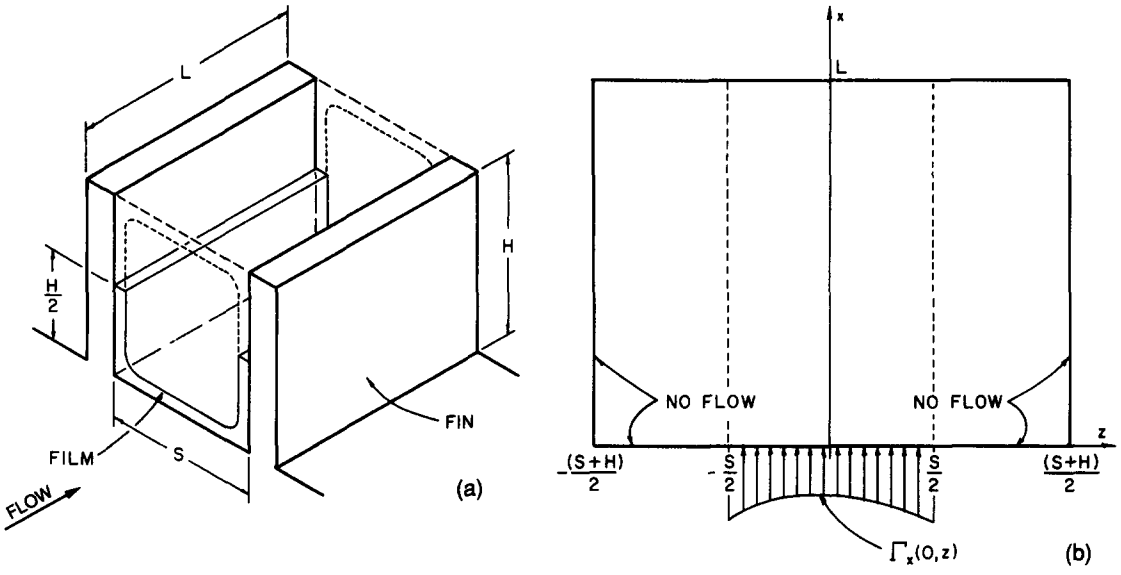

Figure 5. Computational domain used for determining the rate of film spreading in the matrix: (a) location of the film in the fin matrix; (b) "unfolded" film used for the computations.

By combining [11] and [12], Γ_z can be eliminated from the continuity equation, leaving

$$\frac{\partial \Gamma_x}{\partial x} = \beta^2 \frac{\partial^2 \Gamma_x}{\partial z^2}. \qquad [13]$$

When [13] is solved subject to the appropriate boundary conditions, the following expression is obtained:

$$\Gamma_x(x, z) = \frac{M_{\text{FILM}}}{S+H} + \sum_{n=1}^{\infty} c_n \exp\left[-\left(\frac{2n\pi\beta}{S+H}\right)^2 x\right] \cos\left(\frac{2n\pi z}{S+H}\right), \qquad [14]$$

with

$$c_n = \frac{2M_{\text{FILM}}}{\pi n S} \sin\left(\frac{n\pi S}{S+H}\right).$$

This equation represents the local variation in the axial mass flow rate per unit length of channel perimeter throughout the flow domain shown in figure 5(b). The streamwise variation in the film flow rate along the prime and secondary surfaces of the channel, $M_{\text{P(PRIME)}}(x)$ and $M_{\text{FIN(PRIME)}}(x)$, respectively, can be found by integrating [14] across the appropriate segment of the channel perimeter. The complete derivation of [14] and closed-form expressions for $M_{\text{P(PRIME)}}$ and $M_{\text{FIN(PRIME)}}$ are presented in the appendix.

3.3. Droplet deposition and entrainment

The contribution of droplet depositon to the film flow rate is quantified using a modified form of the deposition model proposel by Robertson (1984). Robertson related the cumulative amount of liquid deposited along the fin wall liquid film, $M_{\text{DROP(FIN)}}(x)$, to the flow rate of fluid (both liquid and vapor), Q_{T}, in the core of the fin matrix through the relation:

$$M_{\text{DROP(FIN)}}(x) = M_{\text{DROP(CORE),O}}\left[1 - \exp\left(-\frac{K_{\text{D}} H}{Q_{\text{T}}} x\right)\right]. \qquad [15]$$

The quantity $M_{\text{DROP(CORE),O}}$ represents the droplet flow rate prior to the initiation of deposition, H is the fin height and K_{D} is a mass transfer coefficient. In computing $M_{\text{DROP(CORE),O}}$, Robertson (1984) assumed that the entire liquid film flowing along the fin wall was dispersed as droplets into the vapor core at the trailing edge of each fin. In the present study, however, some of the fin wall film is assumed to be drawn to the prime surface by surface tension. As a result, the value of $M_{\text{DROP(CORE),O}}$ used here is slightly different from that used by Robertson. More specifically,

$M_{DROP(CORE),O}$ reflects the influence of surface tension on the film fluid mechanics at the trailing edge of the fins in the matrix.

In a recent study of droplet shedding phenomena in offset fin geometries, Mandrusiak & Carey (1990) postulated that only liquid which flowed in a central "entrainment region" could potentially be shed into the vapor core as droplets (figure 6). They argued that, for entrainment to occur, the distance over which surface tension forces influenced film behavior, L_c, could not exceed half the fin height (i.e. $L_c < H/2$). This condition was expressed mathematically in terms of a threshold value of a Weber number, We_H^*, parameter, where $We_H = G^2x^2H/\rho_G\sigma$ (G being the total mass flux):

$$\frac{L_c}{\frac{H}{2}} = \frac{We_H^*}{We_H} < 1 \quad \text{for entrainment to occur.} \qquad [16a]$$

They also postulated that, for some conditions, the liquid film may be too thin to allow entrainment from the fins to continue. This condition was also characterized by a critical value of the Weber number We_δ^*, this time based on the film thickness, δ(i.e. $We_\delta = G^2x^2\delta/\rho_G\sigma$):

$$We_\delta > We_\delta^* \quad \text{for entrainment to occur.} \qquad [16b]$$

Experimental data obtained by these investigators appeared to support their assertion that entrainment only occurred over a certain range of flow conditions and was negligible outside of this range.

The model proposed by Mandrusiak & Carey (1990) considers conditions at the point of *incipient* entrainment of droplets from the fins. It may also, however, provide a means of predicting the droplet flow rate once entrainment begins. Let $M_{FIN(END)}$ denote the flowrate of liquid on the fin walls at the trailing edge of the fin and let M_{SHED} be the amount of this film which is shed as droplets. If the film is uniformly distributed across the fin height, then the fraction shed is, to a first approximation (figure 6):

$$\frac{M_{SHED}}{M_{FIN(END)}} = \frac{H - 2L_c}{H}. \qquad [17]$$

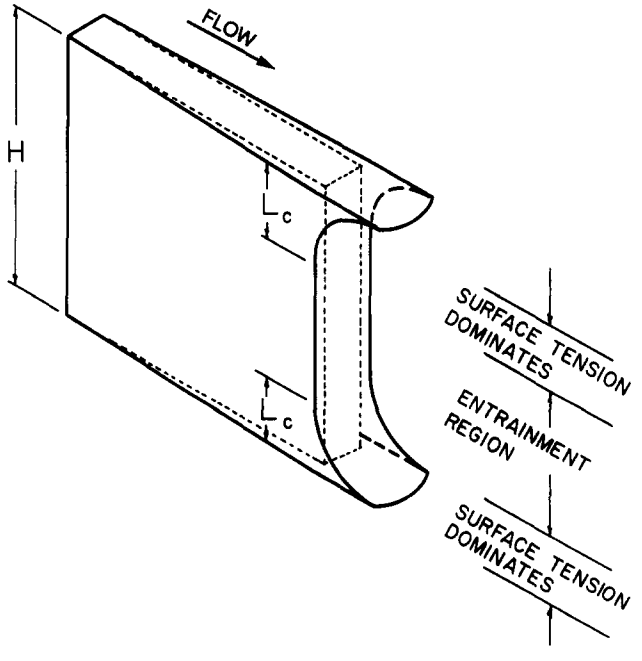

Figure 6. Identification of the "entrainment region" at the trailing edge of a fin. Droplet entrainment is assumed to occur from this section of a fin only (Mandrusiak & Carey 1990).

The entrainment model proposed by Mandrusiak & Carey (1990) suggests that L_c/H depends on We_H. For the computational model being developed here, reasonable predictions of two-phase performance characteristics were obtained when L_c/H was computed using the following empirical relation:

$$\frac{2L_c}{H} = \left(\frac{12}{We_H}\right)^{0.2}.$$

Combining this with [17] yields the following expression for the droplet shedding fraction:

$$\frac{M_{SHED}}{M_{FIN(END)}} = 1 - \left(\frac{12}{We_H}\right)^{0.2}. \quad [18]$$

During periodically fully developed annular flow, the amount of liquid shed from the end of each fin must equal the amount deposited along its lateral surface. Consequently, M_{SHED} and $M_{DROP(FIN)}$ are related through [15]:

$$M_{SHED} = M_{DROP(CORE),O}\left[1 - \exp\left(-\frac{K_D HL}{Q_T}\right)\right]. \quad [19]$$

$M_{FIN(END)}$ in [17] must equal the sum of the amounts of liquid transferred to the fin through film spreading, $M_{FIN(PRIME)}(L)$ (see [A.7]), and through droplet deposition from the core, $M_{DROP(FIN)}(L)$ (see [15]):

$$M_{FIN(END)} = M_{FIN(PRIME)}(L) + M_{DROP(FIN)}(L). \quad [20]$$

When [17]–[20] are combined and rearranged, the following expression is obtained for $M_{DROP(CORE),O}$:

$$\frac{M_{DROP(CORE)O}}{M_L} = \left[1 + \left\{\frac{1}{\theta\left[\left(\frac{We_H}{12}\right)^{0.2} - 1\right]}\right\}\left[1 - \exp\left(-\frac{K_D HL}{Q_T}\right)\right]\right]^{-1}. \quad [21]$$

In this equation, $\theta = M_{FIN(PRIME)}(L)/M_{FILM}$ and is calculated using [A.7] (see the appendix) with $x = L$.

4. MOMENTUM AND ENERGY TRANSPORT IN THE LIQUID FILM

The treatment of momentum and energy transport in the liquid film in most previous models of annular flow in offset fin geometries has, in many respects, been the same. The convective terms are usually dropped from the governing equations and the velocity and temperature profiles are assumed to depend only on the cross-film coordinate. The liquid exchange process described in section 3 suggests that the film behavior is more complex than has been assumed previously. An order of magnitude analysis indicates that the acceleration terms in the film Navier–Stokes equation are of the same order as the cross-film shear terms. As a result, the convective terms must be retained in the governing equations for both the velocity and temperature fields in the film. Droplet deposition also complicates the analysis by making the boundary conditions along the gas–liquid interface more complex than has been assumed previously.

The equations governing the velocity and temperature fields in the liquid film flowing along the channel perimeter were developed using the following idealizations:

(1) For the conditions being considered here, the liquid film Reynolds number rarely exceeds 500. Consequently, momentum transport is assumed to be an essentially laminar process along the entire length of the fin matrix.
(2) Lateral variations in the film velocity field are small in comparison to variations in the streamwise direction or across the film thickness.
(3) The effect of surface tension on the pressure variation in the liquid film is negligible.
(4) The thickness of the liquid film is small in comparison to its length and breadth.

(5) The streamwise variation in film thickness is determined solely by the momentum and continuity equations. This assumes that the evaporation rate along a given fin is sufficiently low that it has only a secondary influence on the film thickness variation along the channel wall.

Since the static pressure and interfacial shear stress acting along the prime and secondary surface films are different, momentum transport in each film will be considered separately. Flow in the corners of the fin matrix (where the prime and secondary surfaces meet) is assumed to have no effect on the fluid mechanics of either film. This regions is idealized as a "bridge" across which mass and momentum are exchanged without resistance (figure 7).

Consistent with the above discussion, the equations governing the velocity field in the liquid film flowing along the prime and secondary surfaces of the fin matrix take the following form:

$$\frac{\partial U}{\partial x} + \frac{\partial V}{\partial y} = S_c(x), \qquad [22]$$

$$\rho U \frac{\partial U}{\partial x} + \rho V \frac{\partial U}{\partial y} = -\frac{\partial P}{\partial x} - \rho g + \mu \frac{\partial^2 U}{\partial y^2} + S_m(x), \qquad [23]$$

$$0 = -\frac{\partial P}{\partial y} \qquad [24]$$

and

$$0 = -\frac{\partial P}{\partial z} \qquad [25]$$

The functions $S_c(x)$ and $S_m(x)$ represent mass and momentum sources which arise through the exchange of liquid between the prime and secondary surfaces (see table 2). The quantity $m_{PF}(x)$ is the local mass exchange rate between the prime and secondary surface films (figure 7) and is computed by differentiating [A.7] with respect to x.

The vertical momentum equation [24], and assumption (3) above indicate that the pressure variation in this film is the same as that in the vapor phase adjacent to the gas–liquid interface. For the film flowing along the fin walls, the pressure along the interface, P_F, is provided directly by the two-dimensional numerical model of the vapor core (section 2). Since the vapor core model does not include prime surface effects, the pressure variation along the prime surface film, P_P, cannot be determined directly from the computed vapor flow field. It seems reasonable

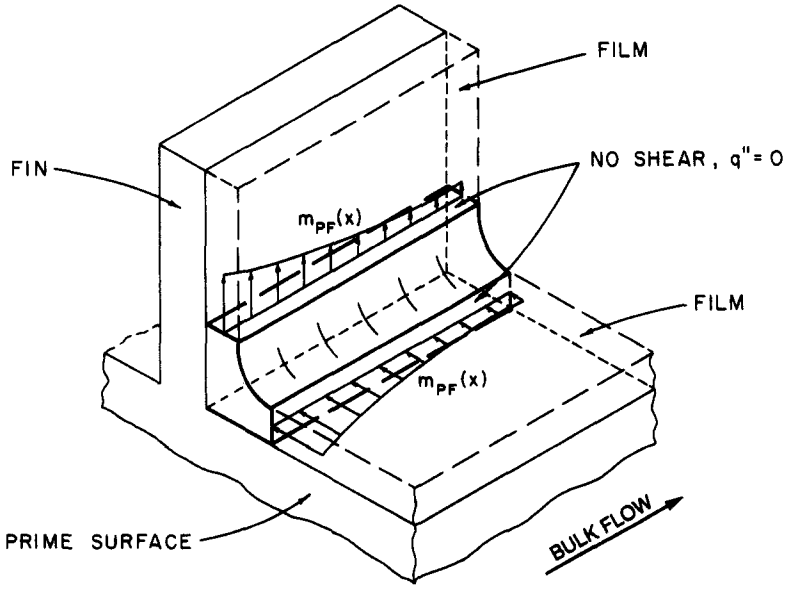

Figure 7. Characteristics of the corner regions of the fin matrix used for the liquid film calculations.

Table 2. Source functions for the continuity and momentum equations

Film	$S_c(x)$	$S_m(x)$
Prime	$-\dfrac{2m_{PF}(x)}{\rho_L S\delta_P(x)}$	0
Secondary	$\dfrac{2m_{PF}(x)}{\rho_L H\delta_F(x)}$	$\dfrac{2m_{PF}(x)}{\rho_L H\delta_F(x)}(\bar{U}_P - \bar{U}_F)$

to expect, however, that flow near the prime surface will experience accelerations and decelerations similar to those of the bulk fluid near the fin midheight. Therefore, the static pressure in the prime surface film was approximated by the integrated mean pressure across the unit cell in figure 2(b):

$$P_P = \frac{1}{S}\int_0^S P_c(x, y)\,dy.$$

It is interesting to note that the momentum source function, $S_m(x)$, only appears in the momentum equation for the film flowing along the fin walls. For this film, the streamwise velocity of liquid entering from the prime surface is different from that of the fin wall film itself, making S_m non-zero. For the prime surface film, however, the momentum per unit mass of liquid leaving the film is the same as that of the film itself making the net momentum loss due to film spreading negligible.

The boundary conditions which must be satisfied by the momentum equations for the prime and secondary surface films are summarized in table 3. The interfacial shear stress variation along the fin wall film, $\tau_{IF}(x)$, is provided directly by the two-dimensional model of the vapor core (section 2). The droplet impingement rate per unit length, $m_{PP}(x)$, required to compute the additional "stress" along the fin wall caused by droplet deposition is computed by differentiating [15] with respect to x. Since the vapor core model does not include prime surface effects, the shear stress along the prime surface film, τ_{IP}, was approximated by values computed using standard correlations for round tube flows:

$$\tau_{IP} = \frac{G^2}{2\rho_G \varepsilon_G^2} f_i,$$

where

$$f_i = 0.005[1 + 75(1 - \varepsilon_G)]$$

and ε_G is the mean void fraction (Wallis 1969).

As a first approximation, the thickness of the fin wall film at the leading edge of the fin is assumed to be zero. This, when combined with [A.2] in the appendix (zero mass flow rate at the leading edge), leads to the inlet boundary condition for the fin wall film shown in table 3. The exact boundary condition which best represents conditions along the inlet to the prime surface film is difficult to specify accurately. The film fluid mechanics at this location is complicated by the liquid exchange processes which occur at the leading and trailing edge of each fin. In addition, the channel flow area is a minimum and the prime surface film flow rate is a maximum at this location. In light of these observations, the prime surface film was assumed to attain its maximum velocity at $x = 0$, leading to the boundary condition, $\partial U_P/\partial x = 0$, shown in table 3.

Table 3. Boundary conditions for the liquid film momentum equations

Location	Prime surface	Secondary surface
$y = 0$	$U_P = 0, V_P = 0$	$U_F = 0, V_F = 0$
$y = \delta(x)$	$\mu_L \dfrac{\partial U_P}{\partial y} = \tau_{IP}(x)$	$\mu_L \dfrac{\partial U_F}{\partial y} = \tau_{IF}(x) + m_{DF}(x)[U_\infty - U_{IF}(x)]$
$x = 0$	$\dfrac{\partial U_P}{\partial x} = 0$	$U_F = 0$

The local film thickness, $\delta(x)$, shown in table 3, was determined using the appropriate local film flow rate M_{Fm} (see the appendix and section 3.1), and the computed film velocity field for each film:

$$M_{Fm}(x) = \int_0^{\delta_m(x)} \rho_L U_m(x, y) L_m \, dy.$$

The dimension, L_m, is equal to the fin height, H, for the fin wall film and to the fin spacing, S, for the prime surface film. The velocity U_m is equal to the spanwise mean U velocity for the fin or the prime surface, as appropriate.

The equation governing energy transport in the liquid film was derived using the following simplifications:

(1) The liquid flowing in the corner regions of the matrix is sufficiently well-mixed by film spreading that lateral conduction effects are negligible.
(2) Axial conduction is small in comparison to transport across the film thickness.
(3) The mean temperature of the prime surface film is approximately the same as that flowing along the fin walls. As such, the exchange of energy which arises through film spreading is small in comparison to the other energy transport processes.

When these idealizations are combined with those presented above for the momentum equation, the energy equation for both the prime and secondary surfaces takes the following form:

$$U\frac{\partial T}{\partial x} + V\frac{\partial T}{\partial y} = \frac{\partial}{\partial y}\left(\alpha_T \frac{\partial T}{\partial y}\right). \qquad [26]$$

For the fluids considered in the present analysis, the Prandtl number, Pr, is sufficiently high that turbulent transport of energy may be significant, even though turbulent transport of momentum was assumed negligible. Consequently, the diffusivity, α_T, in [26] represents the combined effects of molecular and turbulent energy transport:

$$\alpha_T = \alpha_m + \epsilon_H = \alpha_m + \frac{\mathrm{Pr}}{\mathrm{Pr}_t}\frac{\epsilon_M}{\nu}.$$

The turbulent diffusivity, ϵ_M, was evaluated using the thin-film diffusivity model proposed by Blanghetti & Schlunder (1978):

$$\frac{\epsilon_M}{\nu} = -0.5 + 0.5\left\{1 + 0.64y^{+2}\left[1 - \exp\left(-\frac{y^+}{26}\right)\right]^2\right\}^{1/2} \qquad (y \leqslant \delta') \qquad [27a]$$

$$\frac{\epsilon_M}{\nu} = 0.0161\,\mathrm{Ka}^{1/3}\,\mathrm{Re}_f^{1.34}\left[\tau_G^* + \delta^*\left(1 - \frac{y^+}{\delta^+}\right)\right][\delta^+ - y^+] \qquad (y > \delta'), \qquad [27b]$$

where $y^+ = y\sqrt{\tau_w/\rho}/\nu$, τ_w being the wall shear stress, and δ^+ equals y^+ evaluated at $y = \delta$. In [27a, b], δ' is the location in the liquid film where the turbulent diffusivity relation for the lower part of the film, [27a], intersects that for the upper part of the film, [27b]. In [27b], $\mathrm{Ka} = \rho_L^3 g^3(\nu_L^2/g)^2/\sigma^3$, $\mathrm{Re}_f = G(1 - x_m)d_h/\mu_L$ and $\tau_G^* = \tau/(\rho_L - \rho_G)(\nu_L^2/g)^{1/3}$. For these calculations the turbulent Prandtl number, Pr_t, was assigned the value of 0.9. Note that for conditions in which the film is very thin, $\epsilon_M/\nu \to 0$ in [27a, b] and the expression for α_T correctly indicates that turbulent energy transport effects are neglible, i.e. $\alpha_T \approx \alpha_m$.

The boundary conditions which must be satisfied by the energy equation for the prime and secondary surface films are summarized in table 4. Most of these boundary conditions assure

Table 4. Boundary conditions for the liquid film energy equations

Location	Prime surface	Secondary surface
$y = 0$	$T = T_{wP}$	$T = T_{wF}$
$y = \delta(x)$	$T = T_{sat}$	$T = T_{sat}$
$x = 0$	$\frac{\partial T}{\partial x} = 0$	$T = T_{sat}$

continuity of temperature and heat flux at the channel walls and the gas–liquid interface. The boundary condition along the inlet plane ($x = 0$) of the prime surface film assumes that the film is sufficiently well-mixed by the film transfer processes occurring at this location that streamwise diffusive transport of energy is negligible (recall the earlier discussion in connection with the momentum equation).

The equations governing the velocity and temperature fields in the liquid film were non-dimensionalized, discretized and solved over a 60 (x) × 100(y) uniform rectangular grid using an implicit finite difference scheme. Pressure and shear stress information required to complete the prime and secondary surface film flow models was supplied by the vapor flow field calculations described in section 2. Since the variation in film thickness and velocity could not be specified *a priori*, vapor core and liquid film calculations were performed iteratively until the velocity fields in both phases no longer changed.

Once the film velocity calculations had converged, the film energy equation [26] was discretized and solved in non-dimensional form over the same 60 × 100 grid used for the velocity calculations. Since the mean temperature of the fin wall could not be specified without knowledge of the mean fin wall heat transfer coefficient, temperature field calculations for the prime and secondary surface films were performed iteratively. Using an initial estimate of the prime surface temperature, the energy equation was solved to obtain the heat transfer coefficients for both the prime and secondary surfaces of the matrix. The definition of fin efficiency was then used to determine a more representative value of the mean fin wall temperature and the fin film energy equation was re-solved to obtain a more accurate value for the fin heat transfer coefficient. The prime surface temperature was then adjusted and energy equation calculations repeated until the computed total heat transfer rate agreed with that used in the experiments against which the results were being compared.

Flow conditions and offset fin geometries considered during the computations were dictated by the availability of experimental data against which the model could be validated (table 5). Pressure drop calculations were performed for adiabatic two-phase flow using "surface 1" in table 5. Mandrusiak (1988) obtained two-phase pressure drop measurements for this surface using a procedure similar to that of Mandrusiak & Carey (1988). Computations were performed using R-113 as the test fluid for a system operating pressure of 101 kPa (see table 6 for properties). Calculations covered mass flux values from 50 to 150 kg/m^{2}s and qualities ranging from 40 to 90%.

Two-phase heat transfer computations were performed for the geometry tested by Robertson & Lovegrove (1983) ("surface 2" in table 5). Computations were performed using R-11 as the working fluid for a system operating pressure of 550 kPa (see table 6 for properties). Calculations covered mass flux values ranging from 95 to 150 kg/m^{2}s and qualities ranging from 45 to 90%. For these calculations, the fins were assumed isothermal and the flow was assumed to be stable annular flow for all qualities (i.e. dryout did not occur). In addition, the heating power levels considered by Robertson & Lovegrove (1983) were sufficiently low that the effects of evaporation on momentum transport could be neglected, especially over the very short length of the control volume under consideration (6.25 mm).

Since the film model was derived for stable annular flow, computations for both test surfaces were only performed for conditions which corresponded to annular flow on the Hewitt & Roberts (1969) flow regime map. Attempts to extend the calculations into the churn flow regime were unsuccessful. The large amount of liquid in the channel for these conditions appeared to cause convergence problems with the liquid film model, preventing completion of the calculations.

Table 5. Dimensions of fin matrices used for the calculations

Dimension (mm)	Surface 1	Surface 2
t	0.13	0.20
H	9.52	6.35
L	3.18	3.18
S	1.59	1.49
d_h	2.72	2.41

Table 6. Fluid properties of the test fluids used in the calculations

Property	R-113 (101 kPa)	R-11 (550 kPa)
ρ_L(kg/m^3)	1507	1329.7
ρ_G(kg/m^3)	7.46	28.7
c_{PL}(J/kg K)	984	940
h_{LG}(J/kg)	143,800	156,800
μ_L(Pa s)	516×10^{-6}	265×10^{-6}
μ_G(Pa s)	10.77×10^{-6}	13.1×10^{-6}
k_L(W/mK)	0.0705	0.0720
σ(N/m)	0.018	0.012
Pr_L	7.20	3.45

5. DISCUSSION OF RESULTS

5.1. Pressure field and interfacial shear stress

The computed variation in pressure along the unit cell of figure 2(b) for surface 2 is shown in figures 8(a, b). In contrast with the variation seen in round tubes, both the integrated average [figure 8(a)] and near-wall [figure 8(b)] pressure gradients become unfavorable over certain sections of the flow domain. The local changes in the integrated mean pressure are partly a consequence of the periodic changes in flow area (and, thus, flow velocity) at the ends of each row of fins. Along the fin walls, the strong local curvature of the streamlines (figure 9) increases the local static pressure gradient to levels even higher than those of the bulk flow. The results shown in figures (a, b) suggest that annular flow models which assume a favorable pressure gradient throughout the matrix may have limited accuracy.

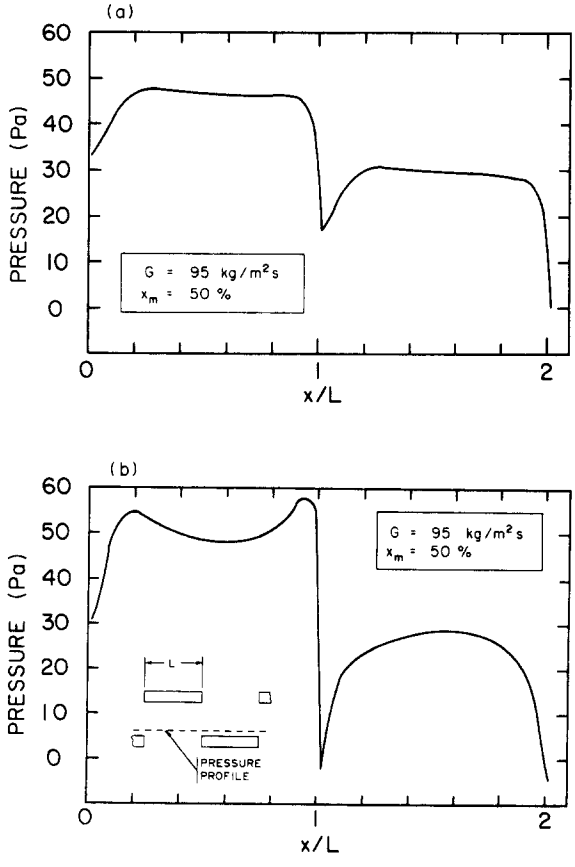

Figure 8. Computed variation of static pressure along the unit cell of figure 2(b): (a) integrated mean pressure; (b) local pressure along the fin walls.

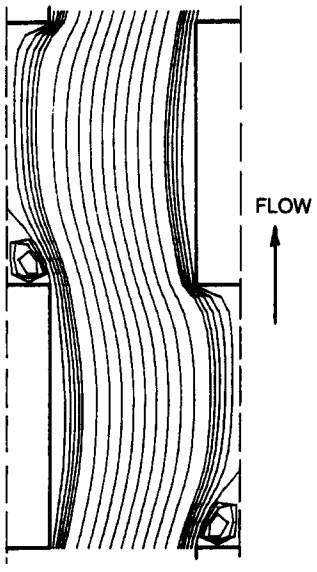

Figure 9. Streamlines near fin walls for a typical set of flow conditions.

During periodically fully developed adiabatic flow, the velocity profile (and, thus, the total momentum flux) across cross-channel planes two fin lengths apart is the same. Consequently, the two-phase pressure gradient in the fin matrix $(dP/dx)_{Ftp}$ can be found using a static force balance over an appropriate segment of the channel [figure 10(a)]:

$$-\left.\frac{dP}{dx}\right|_{Ftp} = \frac{1}{LSH}(F_D + 2LS\bar{\tau}_{wP} + 2LH\bar{\tau}_{wF}). \quad [28]$$

The pressure gradient which results from gravity acting on the liquid film has not been included in [28]. [The small thickness (typically 0.05 mm) of the film makes its associated hydrostatic pressure gradient only a small fraction of the overall gradient given by [28] (<5%).] The mean wall shear stress terms, $\bar{\tau}_{wP}$ and $\bar{\tau}_{wF}$ on the prime and fin surfaces, respectively, were determined by integrating the computed local shear stress variation, $\tau_{wF}(x)$ or $\tau_{wP}(x)$ (as appropriate) along the unit cell:

$$\bar{\tau}_{wF} = \int_0^L \left(\mu_L \left.\frac{\partial U_F}{\partial y}\right|_w\right) dx; \quad \bar{\tau}_{wP} = \int_0^L \left(\mu_L \left.\frac{\partial U_P}{\partial y}\right|_w\right) dx, \quad [29]$$

where U_F and U_P are the U velocity components over the fin and prime surfaces. The fin form drag term in [28], F_D, was approximated by the value determined from the two-dimensional numerical model of the vapor core. For this calculation, the two-dimensional analog to [28] was used to relate the computed pressure drop ΔP_2 to F_D and mean interfacial shear stress, $\bar{\tau}_i$ [figure 10(b)]:

$$F_D = -\Delta P_2 S - 2L\bar{\tau}_i. \quad [30]$$

Although the numerical model presented above was developed for annular two-phase flow, it can be used to study single-phase flow in offset fin geometries by setting the quality, x_m, equal to one. Single-phase pressure drop information predicted for surface 1 (table 5) using the computer model is presented in figure 11. Since experimental friction factor data are not available for this particular surface, the numerical predictions are compared to values computed using the standard correlation proposed by Webb & Joshi (1982). As this figure indicates, the numerical predictions are in excellent agreement with the standard correlations for both laminar and turbulent flow conditions. The slight deviations visible in this figure are likely a consequence of the approximate treatment of prime surface and form drag effects when deriving [28].

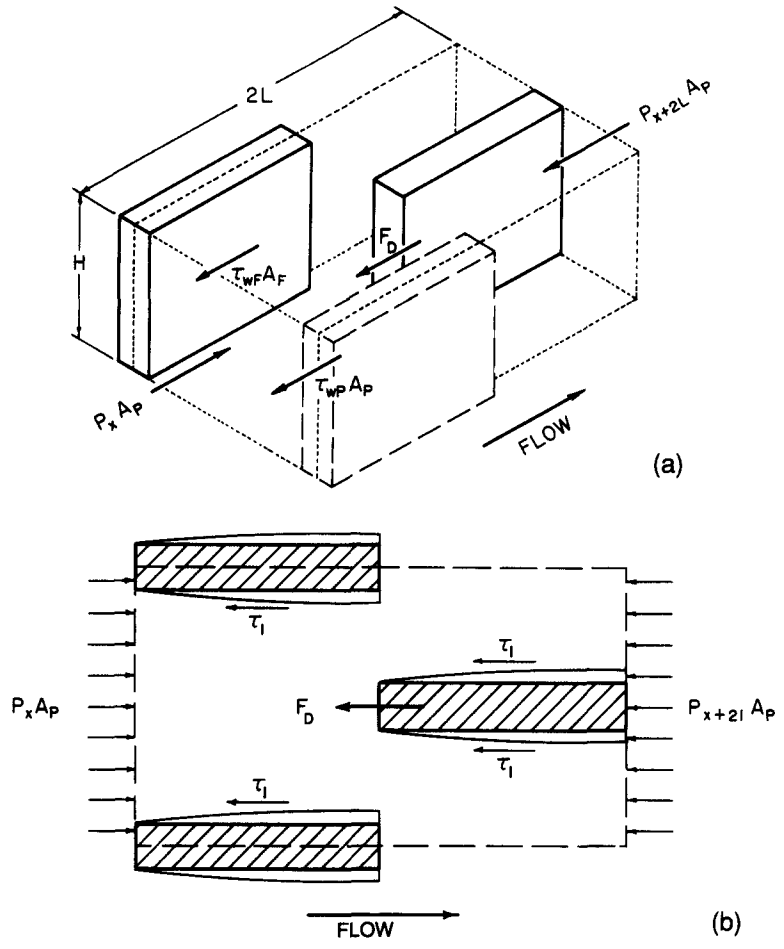

Figure 10. Static force balances to determine pressure drops across the computational unit cell: (a) calculation of the overall pressure gradient; (b) calculation of the fin form drag.

The frictional component of the two-phase pressure gradient ([28]) is often correlated in terms of the two-phase multiplier, ϕ_L, and the Martinelli parameter, X:

$$\phi_L = \left(\frac{\left.\frac{dP}{dx}\right|_{Ftp}}{\left.\frac{dP}{dx}\right|_{FL}} \right)^{1/2}; \quad X = \left(\frac{\left.\frac{dP}{dx}\right|_{FL}}{\left.\frac{dP}{dx}\right|_{FG}} \right)^{1/2}.$$

The subscripts FL and FG designate the frictional pressure gradients for the liquid phase and the vapor phase flowing alone, respectively. The computed variation of ϕ_L with $1/X$ is compared to experimental measurements obtained for surface 1 (table 5) in figure 12. The single-phase gradients needed to computed X and ϕ_L were determined using friction factors from figure 11. Values of ϕ_L predicted by the numerical model are, in general, in good agreement with experiment. The slight underprediction of ϕ_L at high values of $1/X$ may indicate that the droplet entrainment model presented in section 3 is not completely accurate when relatively little liquid is present in the channel. The slight overprediction of ϕ_L at low qualities may suggest that homogeneous flow theory does not accurately model the core flow when the entrained droplet flow rate is relatively high.

The computed variation of shear stress along the interface of the fin wall film is shown in figure 13. The variation in interfacial shear stress is qualitatively similar to that for single-phase flow in these geometries (Patankar & Prakash 1981). The broken line in figure 13 represents the mean interfacial shear stress computed using the round tube correlation proposed by Wallis (1969). The results in this figure suggest that round tube correlations do not accurately represent either the magnitude or variation of interfacial shear stress in geometries of this type.

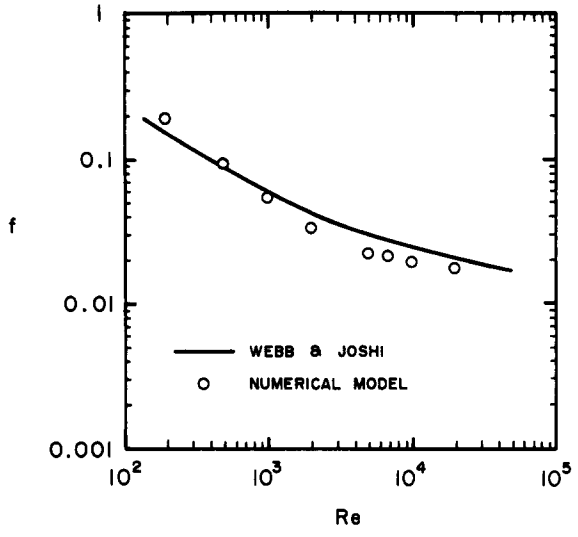

Figure 11. Friction factor variation computed with the numerical model for surface 1 (table 5).

5.2. *Two-phase heat transfer*

Values of the mean two-phase heat transfer coefficients computed for surface 2 (table 5) are compared to experimental data in figure 14. The predicted values of h_{tp} shown in figure 14 were obtained from the computed temperature fields in each film using the following relation to account for the effect of fin efficiency η_F:

$$h_{tp} = \frac{\bar{h}_P A_P + \bar{h}_F \eta_F A_F}{A_P + \eta_F A_F}. \quad [31]$$

Values of $\bar{h}_F$ and $\bar{h}_P$ were obtained by integrating the computed variation of $h_F(x)$ and $h_P(x)$ along the unit cell, where for either surface, h was determined as $h = -\lambda_L(\partial T/\partial y)_{y=0}/(T_w - T_{sat})$, λ_L being the liquid thermal conductivity. The numerical predictions of the two-phase heat transfer coefficient appear to be in excellent agreement with the corresponding experimental measurements.

The computed variation of the two-phase heat transfer coefficient along the prime and secondary surface walls is shown in figure 15(a,b). The variation of h_F along the fin walls [figure 15(a)] is qualitatively similar to that for single-phase flow in offset fin geometries. The high local heat transfer coefficient near the leading edge of the fin is a result of the small thickness (and, consequently, low thermal resistance) of the film at this location. Near the trailing edge, the favorable pressure gradient and high interfacial shear stress combine to accelerate the film towards the end of the fin, reducing its thickness and increasing the local heat transfer rate.

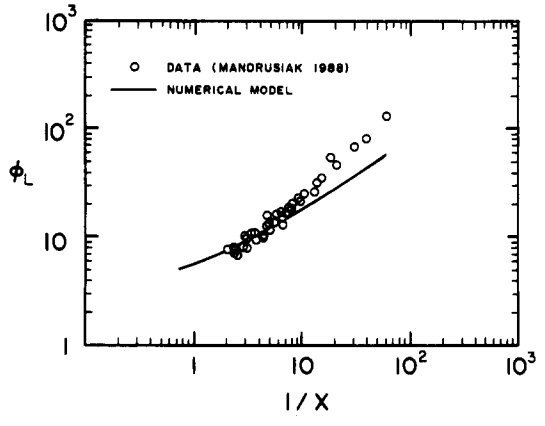

Figure 12. Variation of the two-phase multiplier computed for surface 1 with the numerical model. The circles correspond to measurements obtained by Mandrusiak (1988).

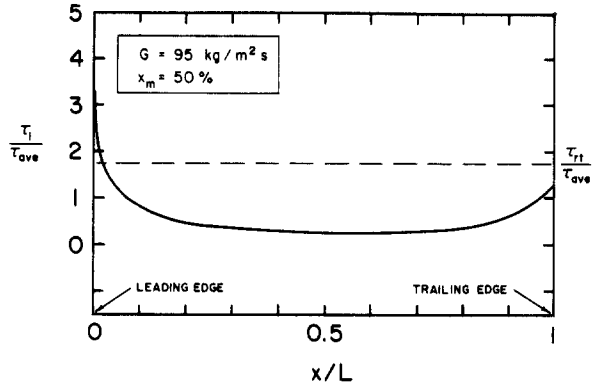

Figure 13. Computed variation of the interfacial shear stress along the film flowing along the fin walls. The broken line corresponds to the mean value computed using the round tube correlation (Wallis 1969).

The streamwise variation of the local heat transfer coefficient along the prime surface [figure 15(b)] is only slightly different from that along the fin wall. Over the first third of the computational unit cell [figure 2(b)], most of the liquid film travels along the prime surface of the matrix. Consequently, the local film Reynolds number is sufficiently high that the heat transfer rate is enhanced by convective transport of energy in the film. As more liquid spreads onto the fin walls, the effects of convective transport becomes smaller and the local heat transfer coefficient is reduced. Near the exit plane of the unit cell, the favorable pressure gradient accelerates the prime surface film, reducing its thickness and increasing the local value of h_P slightly.

The variation in h_P shown in [figure 15(b)] suggests that, for certain conditions, convective energy transport significantly enhances the rate of heat transfer in the liquid film. In an attempt to quantify the importance of convective effects, paired calculations were performed in which the convective terms were alternately included and omitted from the energy equation, for otherwise identical flow conditions. The computed variation of the two-phase heat transfer coefficient along the fin wall is presented for both sets of calculations in figure 16(a). Near the leading and trailing edges of the fin, the film is thin enough that convective energy transport contributes relatively little to $h_F(x)$. In the central part of the fin, however, the film Reynolds number is high enough that convection enhances the local heat transfer coefficient by 20–30% over that by conduction alone. This exercise is repeated for the same flow rate but a higher quality in 16(b). For these conditions, the film Reynolds number is sufficiently low that convective energy transport is negligible in comparison to cross-film conduction all along the fin.

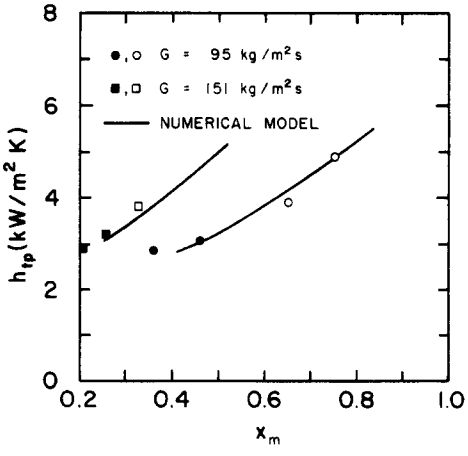

Figure 14. Mean heat transfer coefficients for surface 2 computed using the numerical model for convective boiling of R-11 at 550 kPa. The symbols (□, ■, ○, ●) denote data obtained by Robertson & Lovegrove (1983). The open symbols correspond to annular flow and the solid symbols designate points near the churn–annular transition.

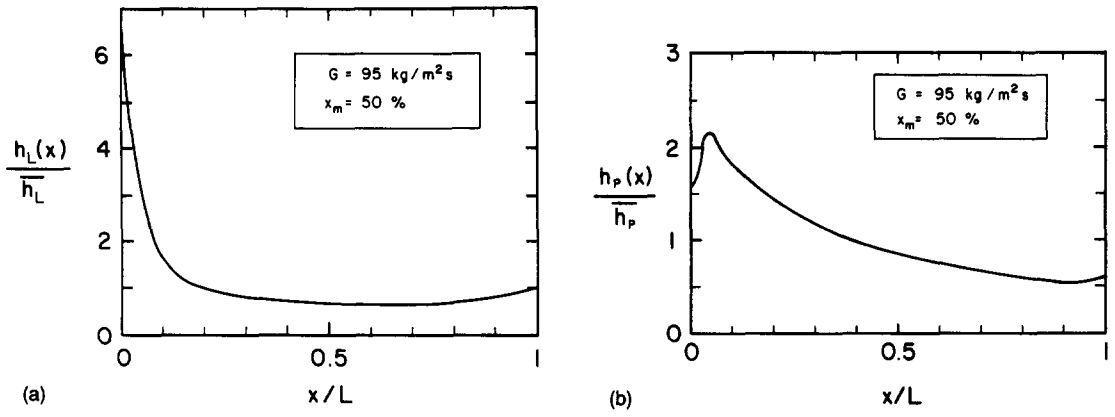

Figure 15. Local variation of the two-phase heat transfer coefficient: (a) along the fin walls; (b) along the prime surface.

These observations suggest that models of annular flow in offset fin matrices which neglect convective energy transport in the liquid film are best-suited to low mass flux or high quality conditions. At moderate qualities and flow rates, the convective terms should be retained in the energy equation to more accurately represent two-phase energy transport in these geometries.

5.3. Effects of channel geometry

Having validated the computational model against measured data, a series of computations were performed to systematically examine the effects of geometry on two-phase transport in offset fin matrices. The effects of channel geometry on the mean heat transfer coefficient are presented in figures 17(a–c). In performing these calculations, the indicated channel dimension was varied while the other two baseline dimensions were held fixed. All computed results shown in figures 17(a–c) and 18(a–c) are for vaporization of R-11 at a saturation pressure of 550 kPa.

The mean heat transfer coefficient appears to increase with increasing fin height [figure 17(a)]. As the fin height increases, the mean thickness of the liquid film flowing along both the prime and secondary surfaces of the channel is reduced. As a result, the thermal resistance of the liquid film drops and the local heat transfer rate goes up. In addition, the enhancement in heat transfer coefficient near the leading edge of the fins contributes more to h_{tp} because the fins comprise a larger fraction of the total channel area.

Increasing the length of the fins in a matrix appears to decrease the mean heat transfer coefficient [figure 17(b)]. This trend is consistent with that reported in the experimental study of two-phase heat transfer by Galezha *et al.* (1976). As the fin length increases, flow in the channel passages becomes similar to that in a continuous-walled tube. As a result, the enhancement in two-phase

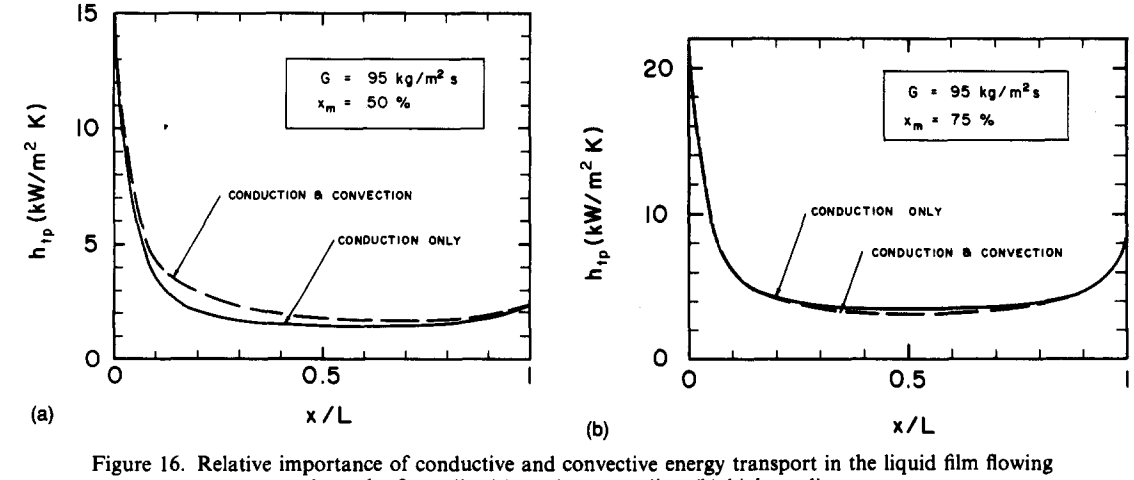

Figure 16. Relative importance of conductive and convective energy transport in the liquid film flowing along the fin walls: (a) moderate quality; (b) high quality.

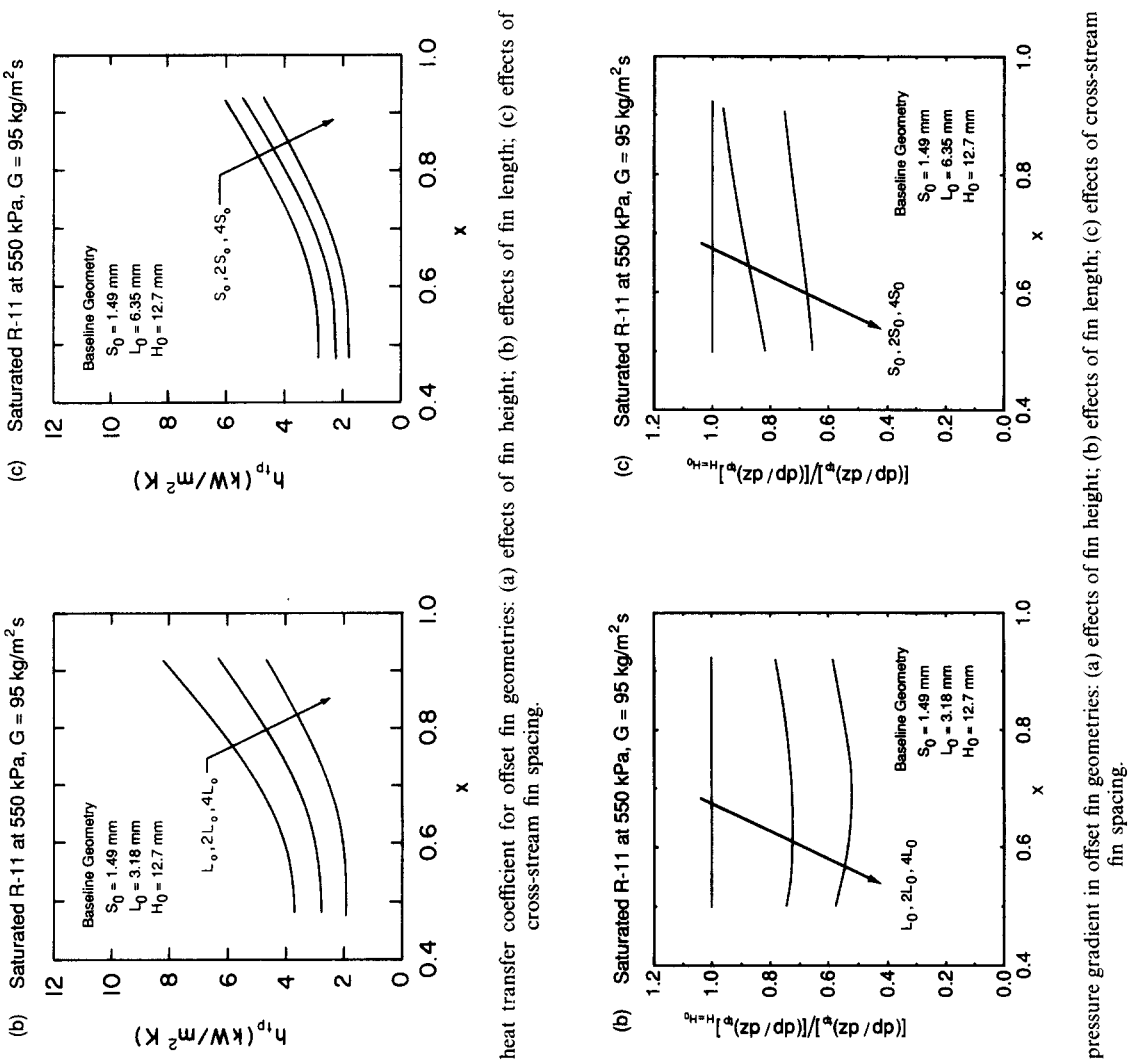

Figure 17. Influence of channel dimensions on the overall heat transfer coefficient for offset fin geometries: (a) effects of fin height; (b) effects of fin length; (c) effects of cross-stream fin spacing.

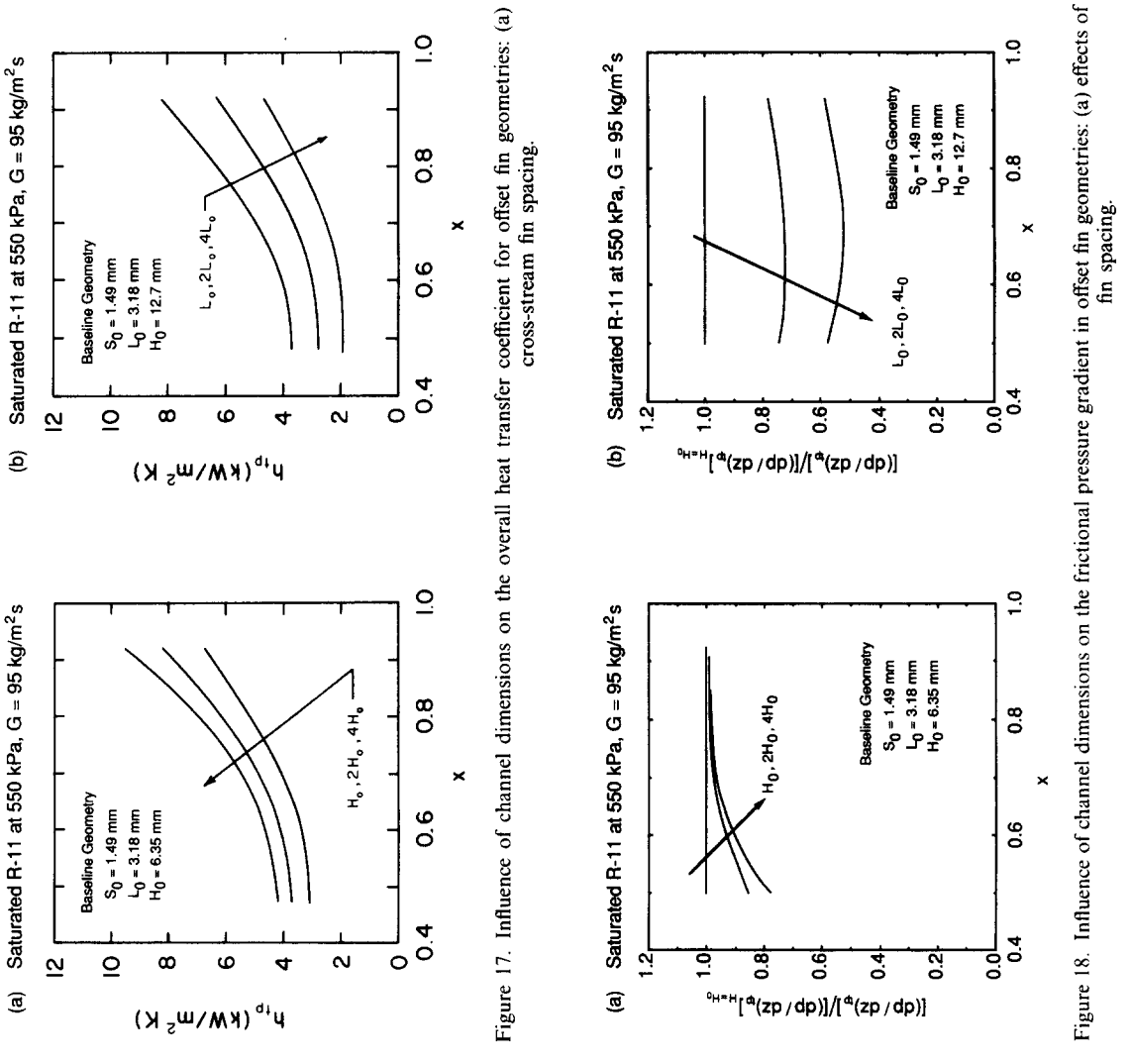

Figure 18. Influence of channel dimensions on the frictional pressure gradient in offset fin geometries: (a) effects of fin height; (b) effects of fin length; (c) effects of cross-stream fin spacing.

heat transfer provided by the fins becomes less important and the overall performance of the surface is diminished.

The results shown in figure 17(c) suggest that the mean heat transfer coefficient decreases as the fins are moved farther apart in the cross-stream direction. When the fin spacing is increased, the fraction of channel area comprised by fins is reduced. As a result, the local enhancement in heat transfer along the fin walls becomes less important in controlling the overall heat transfer coefficient for the matrix. In addition, the mean velocity and thickness of the film flowing along the prime surface are reduced, and the contribution of convective energy transport in the prime surface film becomes less important [recall figure 16(a)].

The effects of channel geometry variations on the two-phase pressure drop characteristics of offset fin matrices, as predicted by our model, are presented in figures 18(a–c). The results shown in these figures cover the same range of flow conditions and channel dimensions as presented in figures 17(a–c). To clearly indicate the effect of the geometry variation, the two-phase pressure gradient in each case has been normalized with that for the baseline geometry at the same flow conditions. (The subscript $H = H_0$ designates the pressure gradient determined for the indicated baseline conditions.) While changes in both the fin length and the fin spacing appear to have significant effects on the pressure gradient, the effects of fin height are relatively small. More importantly, changes in fin height appear to affect the two-phase heat transfer coefficient and two-phase pressure gradient in opposite ways [cf. figures 17(a–c)]. As a result, increasing fin height simultaneously enhances the heat transfer performance of the surface while reducing its two-phase pressure drop. Changes in fin length and spacing appear to have competing effects on performance—the increase in heat transfer coefficient resulting from reducing the fin length or spacing is offset by an increased pressure drop penalty.

The results of this parametric study suggest that optimal offset fin geometries for two-phase flow performance will tend to have taller fins. The selection of the optimal fin length and spacing appears to depend upon whether the improved heat transfer performance achieved with shorter, more closely-spaced fins warrants the increased two-phase pressure drop. Additional two-phase heat transfer measurements are required for other offset fin geometries to fully validate the theoretical predictions made here.

6. CONCLUSIONS

This paper describes a finite difference model of annular two-phase flow in vertical offset strip fin heat exchanger geometries. In this model, the velocity and pressure fields in the vapor core of the fin matrix were determined by numerically solving the turbulent momentum transport equations with a k–ϵ closure scheme. Computed shear stress and pressure field information was then input to a second model of the liquid film to determine the local variation in the heat transfer rate and wall shear stress all along the matrix walls. Results obtained using this computational model suggests the following conclusions:

(1) Although the model proposed here is the most detailed and most fundamental to date, it was necessary to treat droplet entrainment and liquid transfer from the prime surface semi-empirically. In spite of the idealizations in the model, numerical predictions of both heat transfer and pressure drop in offset fin geometries examined here were in excellent agreement with experimental data.

(2) The model indicates that the local behavior of annular flow in offset fin surfaces is more complicated than that observed in round tubes operating under the same flow conditions. The complex shape of the flow domain causes the variation in interfacial shear stress along the fin film to be non-uniform. The local shear stress near the leading and trailing edges of the fin is typically 2–3 times higher than that near the middle of the fin. In addition, the magnitude of the mean stress was found to be as much as 50% lower than values computed using standard correlations for round tubes. The periodic changes in flow area and sharp turning of the flow as it passes around each fin also generate a region of strongly adverse pressure gradient along the first third of each fin in the matrix. The magnitude of the adverse pressure gradient was often 2–3 times the mean gradient across

the entire fin matrix. Even with the high local shear stress at this location, the pressure gradient was sometimes too large to allow continued downstream flow of the film along the fin walls, expecially for moderate quality conditions. For these conditions, a local value for the film thickness could not be obtained using the film model and the two-phase flow model would not converge.

(3) At low and moderate qualities, convective transport in the film was found to enhance the local heat transfer coefficient by 20–30% over that produced by molecular conduction effects alone. At high qualities, convective energy transport becomes unimportant and most of the heat transfer occurs through cross-film conduction.

(4) The computational model developed here shows promise as a tool for studying the effects of geometry on two-phase transport through offset fin matrices. Theoretical computations performed here suggest that the local heat transfer coefficient in these surfaces increases with increasing fin height and decreases with increasing fin length and cross-stream spacing. The two-phase pressure gradient was found to decrease with increasing fin height, length and cross-stream spacing. These results suggest that taller fins are preferred for optimal performance.

Acknowledgement—Support for this research provided by the National Science Foundation under Grant No. CBT-8451781 is gratefully acknowledged.

REFERENCES

BLANGHETTI, F. & SCHLUNDER, E. U. 1978 Local heat transfer coefficients on condensation in a vertical tube. *Proc. 6th Int. Heat Transfer Conf.* **2,** 437–442.

BUTTERWORTH, D. 1968 Air–water climbing film flow in an eccentric annulus. In *Concurrent Gas–Liquid Flow* (Edited by RHODES, E. & SCOTT, D. S.), pp. 145–201.

BUTTERWORTH, D. 1972 Air–water annular flow in a horizontal tube. *Prog. Heat Mass Transfer* **6,** 239–253.

CAREY, V. P. & BENNETT, W. E. 1985 Pressure drop characteristics of horizontal two-phase flow in offset strip fin geometries at low quality. In *Proc. Natn. Heat Transfer Conf.*, Denver, Colo, pp. 23–44.

CAREY, V. P. & MANDRUSIAK, G. D. 1986 Annular film-flow boiling of liquids in a partially heated, vertical channel with offset strip fins. *Int. J. Heat Mass Transfer* **29,** 927–939.

CHEN, C. C., LOH, J. V. & WESTWATER, J. W. 1981 Prediction of boiling heat transfer duty in a compact plate–fin heat exchanger using the improved local assumption. *Int. J. Heat Mass Transfer* **24,** 1907–1912.

COLLIER, J. G. 1972 *Convective Boiling and Condensation.* McGraw-Hill, New York.

GALEZHA, V. B., USYUKIN, I. P. & KAN, K. D. 1976 Boiling heat transfer with freons in finned-plate heat exchangers. *Heat Transfer Sov. Res.* **8,** 103–110.

GOSMAN, A. D. & IDERIAN, F. J. K. 1976 TEACH-2E: A general computer program for two-dimensional, turbulent, recirculation flows. Dept of Mechanical Engineering, Imperial College, London.

HEWITT, G. F. & ROBERTS, D. N. 1969 Studies of two-phase flow patterns by simultaneous X-ray and flash photography. Report AERE-M 2159.

LAUNDER, B. E. & SPALDING, D. B. 1974 The numerical computation of turbulent flows. *Comput. Meth. appl. Mech. Engng* **3,** 269–280.

MANDRUSIAK, G. D. 1988 Modeling of boiling and two-phase flow in offset strip fin heat exchanger geometries. Ph.D. Dissertation, Mechanical Engineering Dept, Univ. of California, Berkeley.

MANDRUSIAK, G. D. & CAREY, V. P. 1988 Pressure drop characteristics of two phase flow in a vertical channel with offset strip fins. *Expl therm. Fluid Sci.* **1,** 41–50.

MANDRUSIAK, G. D. & CAREY, V. P. 1989 Convective boiling in vertical channels with different offset strip fin geometries. *ASME Jl Heat Transfer* **111,** 156–165.

MANDRUSIAK, G. D. & CAREY, V. P. 1990 Liquid shedding phenomena during annular flow in vertical channels with offset strip fins. *Expl therm. Fluid Sci.* In press.

PANITSIDIS, H., GRESHAM, R. D. & WESTWATER, J. W. 1975 Boiling of liquids in a compact plate–fin heat exchanger. *Int. J. Heat Mass Transfer* **18,** 37–42.

PATANKAR, S. V. 1980 *Numerical Heat Transfer and Fluid Flow.* Hemisphere, New York.

PATANKAR, S. V. & PRAKASH, C. 1981 An analysis of the effect of plate thickness on laminar flow and heat transfer in interrupted-plate passages. *Int. J. Heat Mass Transfer* **24,** 1801–1809.

ROBERTSON, J. M. 1982 The correlation of boiling coefficients in plate–fin heat exchangers passages with a film-flow model. *Proc. 6th Int. Heat Transfer Conf.* **2,** 341–345.

ROBERTSON, J. M. 1984 The prediction of convective boiling coefficients in serrated plate-fin passages using an interrupted liquid-film flow model. *Basic Aspects of Two Phase Flow and Heat Transfer. ASME HTD* **34,** 163–171.

ROBERTSON, J. M. & LOVEGROVE, P. C. 1983 Boiling heat transfer with freon 11 (R11) in brazed aluminum plate–fin heat exchangers. *ASME Jl Heat Transfer* **105,** 605–610.

WALLIS, G. B. 1969 *One Dimensional Two Phase Flow.* McGraw-Hill, New York.

WEBB, R. L. & JOSHI, H. M. 1982 Prediction of the friction factor for the offset strip-fin matrix. In *Proc. ASME–JSME Joint Thermal Engineering Conf.*, pp. 461–469.

YUNG, D., LORENZ, J. J. & PANCHAL, C. 1980 Convective vaporization and condensation in serrated-fin channels. *Heat Transfer in Ocean Thermal Energy Conversion. ASME HTD* **12,** 29–37.

APPENDIX

Calculation of Film Mass Flow Rate

In section 3.1, the mass flow rate per unit length of channel periphery, Γ_x, was shown to satisfy

$$\frac{\partial \Gamma_x}{\partial x} = \beta^2 \frac{\partial^2 \Gamma_x}{\partial z^2}. \qquad [13]$$

The solution to [13] must satisfy the following boundary conditions. In figures 5(a, b), the planes $z = 0$ and $z = \pm(S + H)/2$ are planes of symmetry. As such, the circumferential mass flow rate, Γ_z, must be zero across these planes. This boundary condition can be expressed in terms of Γ_x as (see [12]):

$$\left.\frac{\partial \Gamma_x}{\partial z}\right|_{z=0} = 0; \quad \left.\frac{\partial \Gamma_x}{\partial z}\right|_{z=(S+H)/2} = 0. \qquad [A.1]$$

Along the inlet plane ($x = 0$), all liquid flowing as a film is assumed to be uniformly distributed across the width of the prime surface ($-S/2 < z < S/2$), with none flowing along the fin walls. If the total film-flow rate is denoted by M_{FILM}, then the boundary condition on Γ_x along the plane $x = 0$ takes the form

$$\Gamma_x(0, z) = \begin{cases} 0, & z \leqslant -\dfrac{S}{2}, \\ M_{\text{FILM}}/2S, & -\dfrac{S}{2} < z < \dfrac{S}{2}, \\ 0, & \dfrac{S}{2} \leqslant z. \end{cases} \qquad [A.2]$$

The quantity M_{FILM} is not to be confused with the total liquid flow rate in the channel, M_{L}. M_{L} includes liquid flowing both as a film along the walls (M_{FILM}) and as droplets in the vapor core ($M_{\text{DROP(CORE),O}}$).

Equations [13], [A.1] and [A.2] are in a form amenable for solution by separation of variables. When these calculations are performed, the following expression is obtained for $\Gamma_x(x, y)$:

$$\Gamma_x(x, z) = \frac{M_{\text{FILM}}}{S + H} + \sum_{n=1}^{\infty} c_n \exp\left[-\left(\frac{2n\pi\beta}{S + H}\right)^2 x\right] \cos\left(\frac{2n\pi z}{S + H}\right); \qquad [A.3]$$

with

$$c_n = \frac{2M_{\text{FILM}}}{\pi n S} \sin\left(\frac{n\pi S}{S+H}\right).$$

To compute the local film-flow rate along the prime and secondary surface walls, [A.3] is integrated across the appropriate segment of the channel perimeter. For the film flowing along the prime surface,

$$M_{\text{P(PRIME)}}(x) = \int_{-S/2}^{S/2} \Gamma_x(x, y)\, dz. \qquad [A.4]$$

Substitution of [A.3] into [A.4] yields

$$\frac{M_{\text{P(PRIME)}}(x)}{M_{\text{FILM}}} = \frac{S}{H+S}\left\{1 + \frac{2(S+H)^2}{\pi^2 SH}\sum_{n=1}^{\infty}\frac{1}{n^2}\sin^2\left(\frac{n\pi S}{S+H}\right)\exp\left[-\left(\frac{2n\pi\beta}{S+H}\right)^2 x\right]\right\}. \qquad [A.5]$$

Similarly, the local film-flow rate due to film spreading along the fin walls is given by

$$M_{\text{FIN(PRIME)}}(x) = 2\int_{S/2}^{(S+H)/2} \Gamma_x(x, z)\, dz. \qquad [A.6]$$

The additional factor of 2 appears in this equation because liquid spreads onto the fin walls from both the front and back walls of the channel. Introducing [A.3] yields

$$\frac{M_{\text{FIN(PRIME)}}(x)}{M_{\text{FILM}}} = \frac{H}{H+S}\left\{1 - \frac{2(S+H)^2}{\pi^2 SH}\sum_{n=1}^{\infty}\frac{1}{n^2}\sin^2\left(\frac{n\pi S}{S+H}\right)\exp\left[-\left(\frac{2n\pi\beta}{S+H}\right)^2 x\right]\right\}. \qquad [A.7]$$

Calculation of the film spreading rate given by [A.5] and [A.7] requires the total film-flow rate prior to the onset of droplet deposition, M_{FILM}. If the rate of vaporization is assumed small in comparison to other liquid transfer processes, then the total liquid flow rate along the unit cell of figure 2(b) will be constant. Consequently, the total liquid film flow rate is related to the total liquid flow rate, M_{L}, and the droplet flow rate prior to deposition, $M_{\text{DROP(CORE),O}}$, by

$$M_{\text{FILM}} = M_{\text{L}} - M_{\text{DROP(CORE),O}}.$$

$M_{\text{DROP(CORE),O}}$ is given by [21].

The streamwise variation in film-flow rate given by [A.4] and [A.5] does not include the contribution from droplet deposition given by the equations in section 3.2. Since the prime surface is continuous in nature, droplet deposition along the prime surface film is assumed to be exactly balanced by entrainment (equilibrium flow). As such, the mass flow rate along the prime surface, $M_{\text{PRIME}}(x)$, is controlled solely by the rate of film spreading and is represented by [A.4]:

$$M_{\text{PRIME}}(x) = M_{\text{P(PRIME)}}(x).$$

Along the fin walls, however, the periodic interruption of droplet deposition by the staggered fins causes an imbalance in the relative rates of deposition and entrainment. Consequently, the fin wall film-flow rate given by [A.7] must be supplemented by the deposition rate given by [15]:

$$M_{\text{DROP(FIN)}}(x) = M_{\text{DROP(CORE),O}}\left[1 - \exp\left(-\frac{K_D H}{Q_{\text{T}}}x\right)\right],$$

so that

$$M_{\text{FIN}}(x) = M_{\text{FIN(PRIME)}}(x) + M_{\text{DROP(FIN)}}(x).$$